

The First Detection of CH₂CN in a Protoplanetary Disk

ALESSANDRA CANTA,¹ RICHARD TEAGUE,¹ ROMANE LE GAL,^{1,2,3} AND KARIN I. ÖBERG¹

¹Center for Astrophysics / Harvard & Smithsonian, 60 Garden Street, Cambridge, MA 02138, USA

²Univ. Grenoble Alpes, CNRS, IPAG, F-38000 Grenoble, France

³IRAM, 300 rue de la piscine, F-38406 Saint-Martin d'Hères, France

ABSTRACT

We report the first detection of the molecule cyanomethyl, CH₂CN, in a protoplanetary disk. Until now, CH₂CN had only been observed at earlier evolutionary stages, in the giant molecular clouds TMC-1 and Sgr 2, and the prestellar core L1544. We detect six transitions of ortho-CH₂CN towards the disk around nearby T Tauri star TW Hya. An excitation analysis reveals that the disk-averaged column density, N , for ortho-CH₂CN is $(6.3 \pm 0.5) \times 10^{12} \text{ cm}^{-2}$, which is rescaled to reflect a 3:1 ortho-para ratio, resulting in a total column density, N_{tot} , of $(8.4 \pm 0.7) \times 10^{12} \text{ cm}^{-2}$. We calculate a disk-average rotational temperature, $T_{\text{rot}} = 40 \pm 5 \text{ K}$, while a radially resolved analysis shows that T_{rot} remains relatively constant across the radius of the disk. This high rotation temperature suggests that in a static disk and if vertical mixing can be neglected, CH₂CN is largely formed through gas-phase reactions in the upper layers of the disk, rather than solid-state reactions on the surface of grains in the disk midplane. The integrated intensity radial profiles show a ring structure consistent with molecules such as CN and DCN. We note that this is also consistent with previous lower-resolution observations of centrally peaked CH₃CN emission towards the TW Hya disks, since the observed emission gap disappears when convolving our observations with a larger beam size. We obtain a CH₂CN/CH₃CN ratio ranging between 4 and 10. This high CH₂CN/CH₃CN is reproduced in a representative chemical model of the TW Hya disk that employs standard static disk chemistry model assumptions, i.e. without any additional tuning.

Keywords: astrochemistry — protoplanetary disk — pre-biotic astrochemistry — surface ices — T Tauri stars

1. INTRODUCTION

The composition of planets, and therefore their suitability to host biological life, is largely dictated by the physical structure and chemical composition of ice and dust grains in the protoplanetary disks surrounding young stars (e.g., Nomura et al. 2016; Andrews et al. 2012). Nitriles are of specific interests since they have, in fact, often been identified as key precursors in the synthesis of RNA and amino acids (Powner et al. 2009; Patel et al. 2015). Observations of comets and meteors reveal that molecules such as HCN and CH₃CN were present in the chemical environment of our early Solar Nebula, and were likely available for prebiotic reactions (Mumma & Charnley 2011; Altwegg et al. 2020). Nitrile existence in both our early Solar system and in the disks of young stars has implications for our understanding of the trajectory of the organic chemistry as it evolves during planet formation. This is important to estimate the organic inventory on newly-formed planets and to

determine what factors contribute to the chemical habitability of nascent planets (Bergner et al. 2018).

HCN and CN were among the first compounds to be observed in a protoplanetary disk, and since their detection in 1997 over 25 new species have been identified in disks (Kastner et al. 1997; McGuire 2018). However, it was not until the advent of ALMA that more complex molecules such as acetonitrile, CH₃CN, and methanol, CH₃OH, were observed (Öberg et al. 2015; Walsh et al. 2016). Other nitriles that have been detected include HNC and cyanopolyne, HC₃N, as well as various isotopologues of HCN and CN, including H¹³CN, HC¹⁵N, DCN and C¹⁵N (Dutrey et al. 1997; Chapillon et al. 2012; Guzmán et al. 2015; Qi et al. 2003; Hily-Blant et al. 2017). Together these nitriles constitute a substantial fraction of the detected organics in disks, which points to an interesting variations in chemical composition at different stages of a star's life: the early stellar stages seem to have significantly less oxygen-rich species than protoplanetary disks (Öberg & Bergin 2020). This

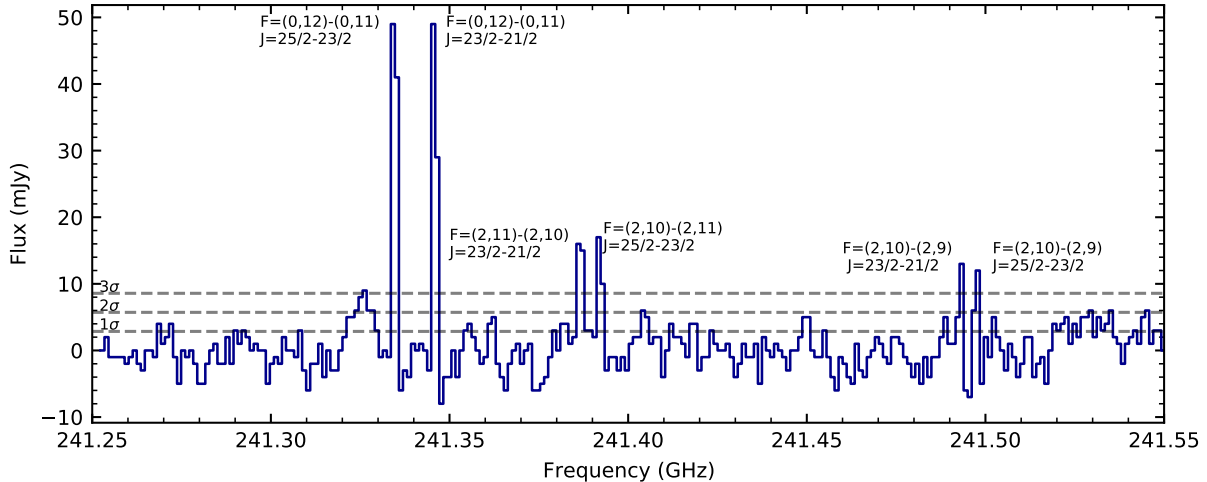


Figure 1. Spectrum of the observed CH_2CN transitions. The 6 brightest peaks are shown with their quantum numbers. The noise is calculated to be 2.9 mJy, with the horizontal dashed lines showing 1, 2 and 3 σ levels.

could be as a result of the oxygen being locked up in molecules such as CO and H_2O and thus unavailable for chemistry, or of a generally oxygen-poor grain-surface chemistry (Oberg & Bergin 2020).

The formation of complex organic molecules (COMs) in protoplanetary disks can happen via two distinct pathways: through grain-surface or gas-phase reactions. Freeze-out reactions on the surface of grains seem to be the greatest contributors to the abundance of COMs in disks, and they involve the absorption of UV radiation from both the central star and the interstellar radiation field (ISRF), formation of radicals and subsequent rearrangement into more complex organics (Oberg 2016). Gas-phase reactions are dominated by a variety of reactions including radiative association (molecules collide and emit a photon), neutral-neutral and neutral-ion reactions and dissociative recombination, where a positive ion recombines with an electron. This was found to be the main reaction pathway for the formation of CH_3CN in TW Hya and of CH_2CN in the protostellar core L1544 (Loomis et al. 2018a; Vastel et al. 2015). Whether this is also the case for CH_2CN in disks has not previously been possible to evaluate since there have been no reported observations of this molecule.

In this paper, we report the first observation of the molecule CH_2CN (in its ortho state) in a protoplanetary disk, specifically in the disk around the nearby T Tauri star TW Hya. This molecule has previously been observed in diffuse molecular clouds SgrB2 and TMC-1, in the pre-stellar core L1544, and in the circumstellar envelope surrounding the star IRC +10216 but never in a protoplanetary disk (Vastel et al. 2015; Irvine et al. 1988; Agúndez et al. 2008). Liszt et al. (2018) also attempted to place upper limits on the abundance of CH_2CN in

diffuse molecular gas. TW Hya is a $\sim 0.8M_\odot$ solar-like T Tauri star that is often used in astrochemical observations because of its proximity (60.1 pc Bailer-Jones et al. 2018) and its face-on orientation, $i \approx 5^\circ$, which allows for easier interpretation of the data. The details of the detection, the data reduction and the observational results are outlined in §2. In §3, we proceed by using a disk-averaged rotational diagram analysis to obtain the total column density for ortho- CH_2CN and an excitation temperature. We also perform a radially resolved analysis to obtain radial profiles for both these parameters. In §4 we compare our findings to a chemical model of TW Hya, which we use to complement our discussion of the chemistry of both CH_3CN and CH_2CN . Finally, we present a summary of our findings in §5.

2. OBSERVATIONS

These observations were taken as part of an ALMA project 2018.A.00021 (PI: Teague), designed to observe ^{12}CO (2-1), CS (5-4) and CN (2-1) emission at high spatial and spectral resolution from the disk around TW Hya (J2000 R.A. 11h01m51.905s, Decl. -34d42m17.03s). The correlator set-up included a single frequency divided mode (FDM) window centered on 241.5 GHz to provide continuum on which to self-calibrate. In this window six strong emission lines were detected and identified as CH_2CN lines, and a single C^{34}S line.

2.1. Data Reduction

The data consists of six executions, two in a compact configuration with baselines spanning 15 m – 500 m on April 4th 2019, and four in a more extended configuration with baselines ranging between 15 m and 2.62 km on September 29th 2019. The shorter baseline executions

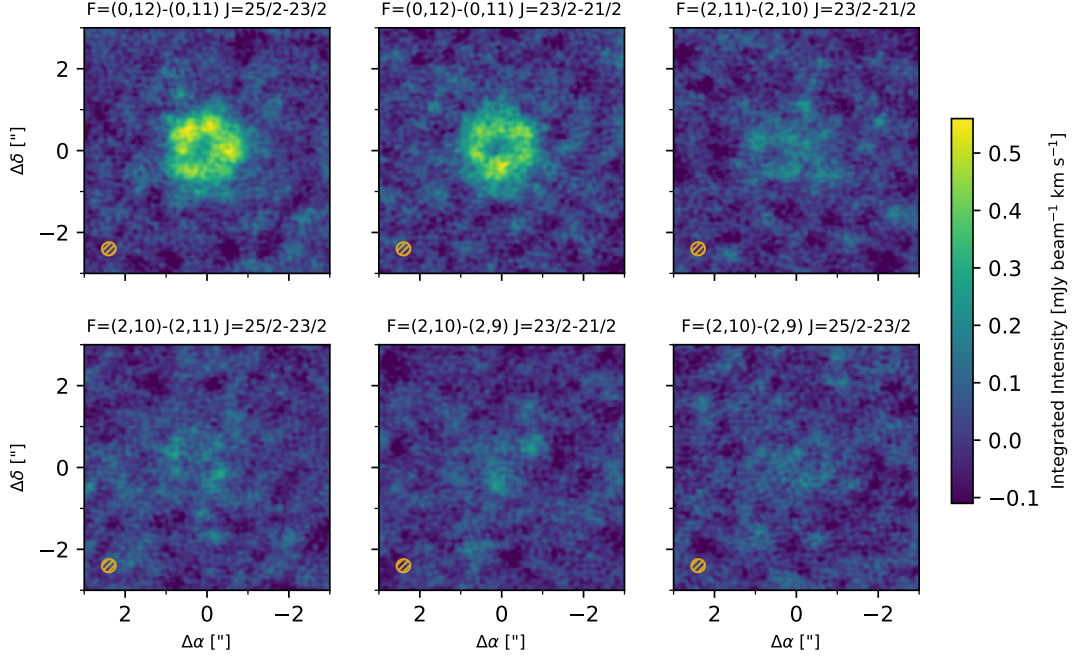


Figure 2. Integrated intensity images of individual observed transitions. All the panels share the same intensity scale. The synthesised beam is shown in the bottom left corner. We find σ to be $0.06 \text{ mJy beam}^{-1} \text{ km s}^{-1}$.

Table 1. Observed CH_2CN Transitions

$N' - N''$	K_a	K_c	$J' - J''$	ν_0	g_u	A_{ul}	$S_{ij}\mu^2$	E_{upper}	Int. Flux Density
				(GHz)		(s^{-1})	(D^2)	(K)	(mJy km s^{-1})
12-11	0 - 0	12 - 11	25/2 - 23/2	241.3335423	234	9.62×10^{-4}	1376.0	75	126.1 ± 6.0
12-11	0 - 0	12 - 11	23/2 - 21/2	241.3458390	216	9.59×10^{-4}	1265.6	75	109.3 ± 6.0
12-11	2 - 2	11 - 10	23/2 - 21/2	241.3860255	216	9.33×10^{-4}	1230.5	128	43.4 ± 6.0
12-11	2 - 2	11 - 10	25/2 - 23/2	241.3913950	234	9.36×10^{-4}	1337.7	128	37.8 ± 6.0
12-11	2 - 2	10 - 9	23/2 - 21/2	241.4925510	216	9.34×10^{-4}	1230.6	128	$25.2 \pm 6.0^{\text{a}}$
12-11	2 - 2	10 - 9	25/2 - 23/2	241.4970603	234	9.37×10^{-4}	1337.7	128	25.2 ± 6.0

NOTE—All data for column $N' - N''$ through to E_{upper} was obtained from The Cologne Database for Molecular Spectroscopy (CDMS; Müller et al. 2001).

^aThis peak includes two distinct transitions: the one that we observe and the another one associated with para- CH_2CN . The latter has a significantly lower A_{ul} ($\sim 3.5 \times 10^{-6} \text{ s}^{-1}$), thus we assume that all the integrated flux observed comes from the ortho line Endres et al. (2016).

included 41.7 minutes on-source integration while the longer baseline executions used 51.1 minutes on-source for a total on-source time of 4.9 hours. The quasar J1037-2934 was used for both bandpass and flux calibration for all executions while the phase calibration was performed with J1147-3812 for the short baseline data and J1126-3828 for the long baseline data.

Initial calibration was performed using the standard pipeline procedure in CASA v5.6.2 (McMullin et al. 2007). The data were then self-calibrated following the self-

calibration procedure used in the DSHARP program (Andrews et al. 2018). In brief, all spectral windows were used, masking out any lines in each spectral window. These line-free observations were used to solve for the phase solutions which were then applied to the entire dataset. Prior to combining the different executions, the executions were aligned to the same phase center and the continuum fluxes were compared. All executions yielded fluxes that were within 2% of one another, except for the final long baseline execution which varied by about 10%.

The final long baseline execution was rescaled using the `gaincal` task such that the total flux matched that of the other three long baseline executions. The continuum was subtracted using the `uvcontsub`.

The continuum FDM window was imaged using the multi-scale CLEAN algorithm and adopting a Briggs weighting with a robust parameter of 2 (similar to natural weighting) yielding a synthesized beam of $0''.34 \times 0''.32$ at a position angle of 104.8° . The data was imaged at the native spectral resolution of the FDM window of 1.4 km s^{-1} .

Figure 1 shows the six detected transitions in the form of three sets of doublets with their associated quantum labelling. Since our emission is not spectrally resolved (due to the spectral-set up and face on orientation of the disk), we were unable to extract our spectra using either a matched filtering approach (e.g., Loomis et al. 2018b) or a line-stacking approach, such as in GoFish (Teague 2019a). The detected transitions are also depicted as integrated intensity (moment-0) maps in Figure 2. While four of the six lines are fairly weak, the two at 241.3335423 and 241.3458390 GHz are robustly detected, exhibiting a clear ring morphology. To better visualize the CH_2CN morphology, we create a high signal-to-noise map by stacking the 6 transitions together. The resulting image is shown in the left panel of Figure 3.

For a more direct comparison with the results presented in Loomis et al. (2018a), we create a version of the images which were smoothed to the same spatial resolution, $1''.05 \times 0''.83$, using the `imsmooth` task in `CASA`. As the weaker transitions are more clearly detected in the smoothed images, we use the smoothed images for both the radially-resolved analysis in §3.3 and the disk-averaged analysis in §3.2. The higher spatial resolution data is only used in the plotting of the channel maps (Figure 2) and of the radial profile (Figure 3) to better constrain the ring morphology.

2.2. Observational Results

The disk-averaged integrated flux measurements reported in Table 1 were obtained by integrating the peaks highlighted in Figure 1 over the two independent 1.5 km/s channels showing emission out to $\sim 2.5''$ (where the intensity reaches 0 in the right panel of Figure 3). Under the assumption of spectrally independent pixels, the uncertainty in the integrated flux is calculated using the equation:

$$\delta M_0 = \sqrt{\sum_{i(I_i > 0)}^N \sigma_i^2 \cdot \Delta v_{\text{chan},i}^2}, \quad (1)$$

where δM_0 indicates the uncertainty in moment-zero (integrated intensity) values; σ_i is the signal-to-noise ratio in the spectrum; and $\Delta v_{\text{chan},i}$ is the channel width (Teague 2019b).

We plot radial profiles to see how the integrated flux changes over the radius of the disk. We radially bin the integrated flux from each transition into $0.05''$ ($\sim 3 \text{ au}$)-wide bins. The beam size was $0.3''$ ($\sim 18 \text{ au}$), therefore our chosen bin size is a sixth of the beam major FWHM. We use a position angle of 152° and an inclination, $i = 5^\circ$ (Huang et al. 2018). We use the native resolution data to plot the radial profile in Figure 3b, which shows the ring morphology quite clearly. For the purpose of our excitation analysis, however, we use the lower spatial resolution smoothed data, with the radial profiles from the individual transitions using this data set shown in Fig. 4B.

The stacked image radial profile shows a ring morphology (Figure 3a), which is also observed in the individual transitions in Fig 2. We fitted the radial profile in Figure 3 with a Gaussian function (Figure 3b) to infer the location of the center of our ring and the ring width. We find the center to be at $0.4''$ ($\sim 24 \text{ au}$) and, full width at half maximum of $1.1''$ ($\sim 69 \text{ au}$). We also see some excess emission between $1.5''$ and $2.5''$ when compared to a single Gaussian ring, however, further characterisation of this feature requires more sensitive observations.

In contrast to the native resolution data, the smoothed data appears to be consistent with a centrally-peaked morphology which is also seen with CH_3CN (Loomis et al. 2018a). The similar distribution suggests a chemical link between the two molecules, which is explored further in Section 4.

3. CH_2CN EXCITATION ANALYSIS

The rotational temperature, T_{rot} , and the total column density of CH_2CN , N , can be constrained through the use of a rotational diagram analysis. This implicitly assumes that the molecular excitation can be described by a single temperature and that the molecules are in local thermodynamic equilibrium (LTE). As we assume that the critical densities for CH_2CN and CH_3CN are similar ($2.0 \times 10^6 \text{ cm}^{-3}$ and $2.6 \times 10^6 \text{ cm}^{-3}$ for the transitions $J = 13 - 12$ and $J = 12 - 11$ at 40 K, respectively), and that chemical models of TW Hya suggest that even atmospheric densities exceed 10^9 cm^{-3} (e.g., Cleaves et al. 2015), it is reasonable to assume that both CH_2CN would be thermalized. As such, we can assume that the excitation temperature is equal to the gas kinetic temperature (Shirley 2015; Guzmán et al. 2018; Loomis et al. 2018a). These parameters allow us to draw conclusions about the physical conditions where CH_2CN

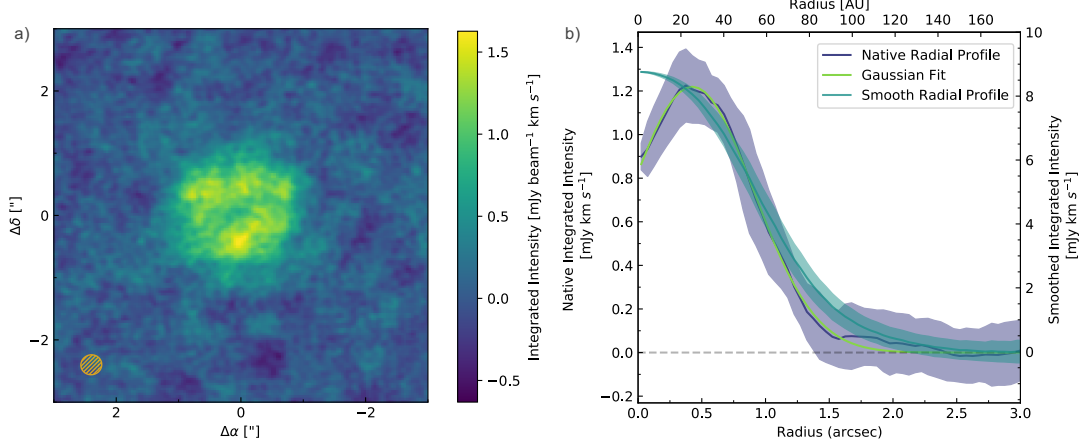


Figure 3. Left panel: Integrated intensity map made from the stacked 6 transitions. The noise is calculated to be $0.14 \text{ mJy beam}^{-1} \text{ km s}^{-1}$. Right panel: the azimuthally averaged integrated intensity radial profile obtained from the stacked native resolution data. Shaded areas represent 1σ uncertainties, where σ represents the standard deviation in each radial bin.

is found and its potential interactions with molecules that exist in a similar environment.

3.1. Method

We start our analysis by constraining the disk-averaged rotational temperature, T_{rot} , and the total column density, N . Following Goldsmith & Langer (1999), we obtain the rotational diagram shown in Figure 4A by using the equation

$$\ln \frac{N_u^{\text{thin}}}{g_u} + \ln C_\tau = \ln N - \ln Q(T_{\text{rot}}) - \frac{E_u}{kT_{\text{rot}}}, \quad (2)$$

where N_u^{thin} is the column density of molecules in the upper state of each transition without the correction for the optical depth effect, C_τ is the optical correction factor, and $Q(T_{\text{rot}})$ is the molecular partition function and E_u is the upper state energy. We use the molecular partition function from The Cologne Database for Molecular Spectroscopy (CDMS; Müller et al. 2001)¹ using a linear interpolation to obtain our Q values (Endres et al. 2016). Degeneracies due to the hyperfine structure are included in the calculation of Q .

We calculate the N_u^{thin} for each transition through the equation:

$$N_u^{\text{thin}} = \frac{4\pi S_\nu \Delta v}{A_{ul} \Omega h c}, \quad (3)$$

where A_{ul} is the Einstein coefficient, S_ν is the disk-averaged integrated flux density calculated as described in §2.2 and using a bin-size of $2.5''$, Δ is the width of the two channels that we used for integration and Ω is the solid angle subtended by the source.

¹ Available at <https://cdms.astro.uni-koeln.de>.

The optical correction factor is obtained through the equation:

$$C_\tau = \frac{\tau}{1 - e^{-\tau}}. \quad (4)$$

where the optical depth, τ , can be related to the upper level population through the equation:

$$\tau_{ul} = \frac{A_{ul} c^3}{8\pi \nu^3 \Delta v} N_u (e^{h\nu/kT_{\text{rot}}} - 1). \quad (5)$$

Given that our emission is dominated by Doppler broadening, the line width, Δv , is given by

$$\Delta v = \sqrt{\frac{2kT_{\text{rot}}}{m_u m_H}}, \quad (6)$$

with m_u being the molecular weight of CH_2CN (40 g/mol) and m_H being the mass of a hydrogen atom.

We create a model that relates N_u , C_τ and Δv to Equation 2 and we derive the values of T_{rot} and N by matching the observed N_u/g_u values. We use Scipy's `curve_fit` function to minimize χ^2 and find the best estimate of our desired parameters (Jones et al. 2001). $\ln(N_u/g_u)$ can then be plotted against the upper state energies, E_u to obtain Figure 4A, where the slope and the y -intercept of the line respectively represent $-T_{\text{rot}}^{-1}$ and N .

3.2. Disk-averaged Analysis

In this paper, we will denote the column density of ortho- CH_2CN using N , whereas the total column density of CH_2CN (including both the ortho and the para isomers) will be indicated using N_{tot} . We obtain a disk-averaged rotational temperature of $40 \pm 5 \text{ K}$ and a disk-averaged total column density, N , of $(6.3 \pm 0.5) \times 10^{12} \text{ cm}^{-2}$ for ortho- CH_2CN . As described in Le Gal

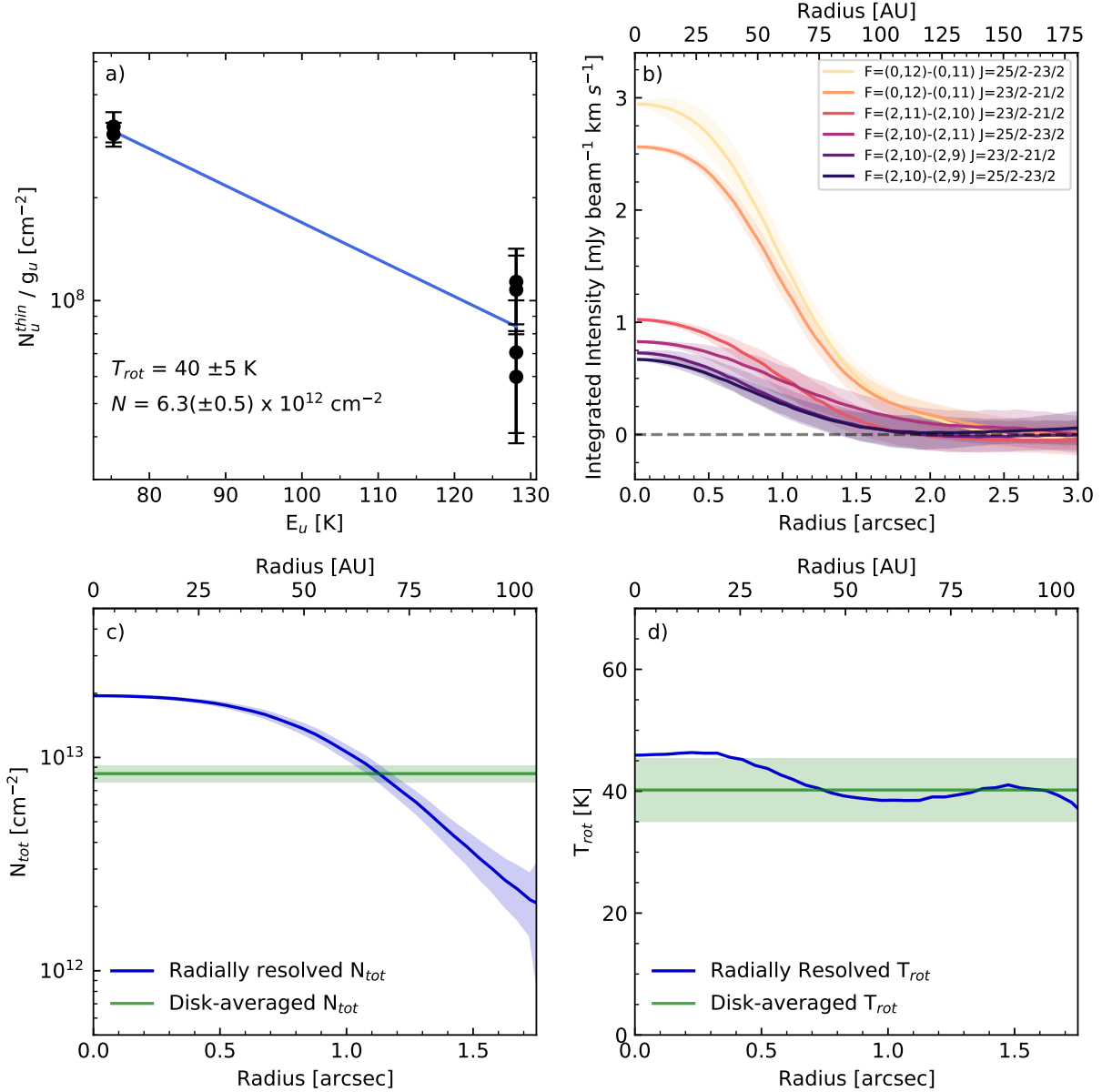


Figure 4. Panel A: ortho-CH₂CN disk-averaged rotational diagram. Panel B: the radial profiles for the six detected transitions. Shaded areas represent 1σ uncertainties. Panels C & D: radial profiles of respectively the CH₂CN total column density and the rotational temperature. The colour dark blue indicates radially resolved values, whereas green is used for values we obtained from disk-averaged analysis. Shaded areas represent 1σ uncertainties.

et al. (2017), for a molecule containing two identical Hydrogen nuclei, such as CH₂CN, we expect a statistical ortho/para ratio of 3:1, and therefore we infer a total column density, N_{tot} , of $(8.4 \pm 0.7) \times 10^{12}$ cm⁻². Indeed, due to the X²B1 symmetry of the ground electronic state of CH₂CN, the ortho-to-para ratio of CH₂CN decreases toward the statistical 3:1 value with increasing temperature as NH₂ (Le Gal et al. 2016). CH₂CN is a heavier molecule than NH₂, therefore, its ortho-to-para ratio will reach the statistical ratio for lower temperatures than NH₂. Thus, according to Fig. 1 of Le Gal

et al. (2016), the relatively high rotational temperature we derived confirms that it is reasonable to consider a 3:1 statistical ortho-para ratio for CH₂CN. Given this ratio, we can calculate the expected para column density and using this value and the expected integrated intensity of the para lines that we do not detect (located at 241.353 and 241.381).

Finally, having obtained T_{rot} , we calculate the optical depth, τ , of our transitions. In all cases, we obtained a value of $\tau \ll 1$, with values of range 4×10^{-4} to 3.4×10^{-3} . Therefore, our detected transitions were

Table 2. Formation and destruction pathways for CH₂CN

Reaction Type	Reactants			Products		Mechanism	Rates of Reaction			
							α [cm ³ s ⁻¹]	β	γ	rate type ^c
Formation	CN	CH ₃	→	H	CH ₂ CN	Neutral-Neutral	1.00(−10)	0.00	0.00	(1)
	N	C ₂ H ₃	→	H	CH ₂ CN	Neutral-Neutral	6.40(−11)	0.17	0.00	(1)
	C	CH ₂ NH	→	H	CH ₂ CN	Neutral-Neutral	1.00(−10)	0.00	0.00	(1)
	CH ₃ CN ⁺	e [−]	→	H	CH ₂ CN	DR ^a	2.00(−7)	−0.50	0.00	(1)
	CH ₃ CNH ⁺	e [−]	→	2 H	CH ₂ CN	DR ^a	8.00(−8)	−0.50	0.00	(1)
	s-CN ^b	s-CH ₂ ^b	→	CH ₂ CN		Grain Surface				
Destruction	CH ₂ CN	C ⁺	→	C	CH ₂ CN ⁺	Ion-Polar	1.00	1.61(−9)	5.81	(2)
	CH ₂ CN	H ₃ ⁺	→	H ₂	CH ₃ CN ⁺	Ion-Polar	1.00	2.94(−9)	5.81	(2)
	CH ₂ CN	hν	→	CN	CH ₂	Photodissociation	1.56(−9)	0.00	1.95	(3)
	CH ₂ CN	hν	→	CH ₂ CN ⁺	e [−]	Photodissociation	5.29(−10)	0.00	3.11	(3)
	CH ₂ CN		→	s-CH ₂ CN ^b		Freeze-out				

NOTE—Table showing all the possible formation and destruction pathways of CH₂CN based on the astrochemical disk model by [Le Gal et al. \(2019\)](#). The rates of reactions are reproduced from the Kinetic Database for Astrochemistry available at <http://kida.astrophy.u-bordeaux.fr> ([Wakelam et al. 2012](#)).

^aDR = Dissociative Recombination

^bs- indicates solid-state reactions, i.e. reactions occurring on the surface of grains.

^cRate formulae (1) Modified Arrhenius Equation $k(t) = \alpha(T/300)^\beta e^{-\gamma/T}$ (2) Ion-polar rate coefficient computed using Su-Chesnavich capture approach $k(t) = \alpha\beta(0.62 + 0.4767\gamma(T/300)^{0.5})$ ([Woon & Herbst 2009](#)) (3) Photo-dissociation reaction rate $k(t) = \alpha e^{-\gamma A_v}$ where A_v is the visual extinction ([Draine 1978a](#); [van Dishoeck 1994](#)).

of negligible optical thickness. In addition to this, using these parameters we can calculate the predicted strength of the lines that we do not detect. For the transitions at 241.353 and at 241.382 (which belong to para-CH₂CN) we obtain integrated intensities of 1.26 and 1.37 mJy km s⁻¹, which are significantly below our calculated intensities, thus confirming that we would not have been able to detect these lines with our spectral set-up. The disk-averaged values obtained in Section 3.1 are calculated out to a radius of 1.75'' as we can see from Figure 4b that at this radius, all six transitions are detected. As a comparison, we calculate an average T_{rot} and N for the outer region of the disk where the weaker emission lines are almost completely lost. For this, we integrated out to a radius of 2.5''. For this outer region, we find a total column density of $(3.5 \pm 0.3) \times 10^{12}$ ($(4.7 \pm 0.4) \times 10^{12}$ for ortho-CH₂CN) cm⁻², and a rotational temperature of 38 ± 5 K. Comparing the total column density that we obtained out to a radius 1.75'' to that out to 2.5'' confirms that the outer radii are contributing very little to the total column density, as we would expect from the radial profiles in Figure 4B and in the right panel of Figure 3.

3.3. Radially Resolved Analysis

To further observe the behaviour of T_{rot} and N_{tot} across the disk, we use the radial integrated intensities from each of the transitions in Figure 4B and we repeat

the steps outlined in Section 3.2 to obtain rotational diagrams at different radii. The results are summarised in panel 4C and D.

Figure 4C shows that the column density decreases from 5×10^{13} to 0.6×10^{13} cm⁻² across the radius of the disk. This is consistent with the disk-averaged column density. The T_{rot} ranges between 45 and 37 K, which is consistent with the disk-averaged T_{rot} (40 ± 5 K). We note that this is very similar to the CH₃CN excitation temperature of $32.7^{+3.9}_{-3.4}$ K in the same disk ([Loomis et al. 2018a](#)). On the other hand, the column density of CH₃CN, $1.82^{+0.25}_{-0.19} \times 10^{12}$ cm⁻², is ~ 10 times lower than our observed CH₂CN's N_{tot} . This is consistent with our chemical model, as discussed in Section 4.1.

4. DISCUSSION

4.1. CH₂CN/CH₃CN Ratio & Disk Models Results

We use the chemical models by [Le Gal et al. \(2019\)](#) to explore the predicted column densities of CH₂CN and CH₃CN as a function of radius, as shown in Figure 4.2a & b. The original model has been modified to fit TW Hya using the physical parameters described in Table 3, and a standard cosmic-ray ionization rate of 1×10^{-17} s⁻¹. We used a C/O ratio of 1 which was the best C/O ratio found in [Le Gal et al. \(2019\)](#) to reproduce the column densities of the nitriles detected in

Table 3. Physical parameters used for the disk chemistry modeling

Parameters	TW Hya ^a
Stellar mass: M_\star (M_\odot)	0.8
Characteristic radius: R_c (AU)	10
Density power-law index	1.5
Midplane temperature at R_c (K)	20
Atmosphere temperature at R_c (K)	104
Surface density at R_c (g cm^{-2})	0.79
Temperature power-law index	0.55
Vertical temperature gradient index	2
UV Flux ^b at R_c (in Draine (1978b) ’s units)	3400

^a [Andrews et al. \(2012\)](#)^b [Herczeg et al. \(2004\)](#)

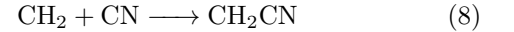
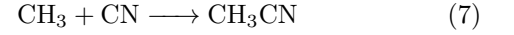
abundance in disks. Overall, the model is in good accordance with our observations as it predicts that CH_2CN is more abundant than CH_3CN at all radii. However, the $\text{CH}_2\text{CN}/\text{CH}_3\text{CN}$ ratio in the model is larger than the ratio of ~ 5 we found observationally. Inspecting Fig. 4.2a&b, we see that the model correctly predicts the column density of CH_2CN and under-predicts that of CH_3CN . This suggests that while the column density of CH_2CN is well reproduced by standard astrochemical model assumptions, there are missing chemical pathways that lead to the formation of CH_3CN . Detailed astrochemical disk modeling effort needs to be made to further constrain the main reaction pathways driving both the observed CH_3CN abundance and $\text{CH}_2\text{CN}/\text{CH}_3\text{CN}$ ratio in the TW Hya protoplanetary disk, but they are beyond the scope of this paper and will be the subject of a future dedicated study. For now, the use of chemical models allows us to confirm that a ratio of $\text{CH}_2\text{CN}/\text{CH}_3\text{CN} > 1$ is indeed plausible in our disk and allows us to give a more comprehensive overview of CH_2CN in TW Hya. Figure 4.2c&d show the abundance distribution of CH_3CN and CH_2CN with respect to height and the radius of TW Hya. Once again, we can see that CH_2CN is more abundant than CH_3CN at all radii and heights in the disk and that the region of brightest emission for both of these molecules is co-localised and between a radius of ~ 50 -100 au and a height of ~ 10 au. This is consistent with our observations as the model in Figure 4.2a shows that our observed N_{tot} for CH_2CN arises from a radius of ~ 100 au.

4.2. CH_2CN Chemistry

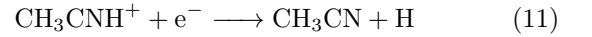
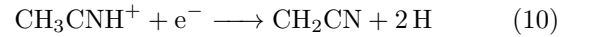
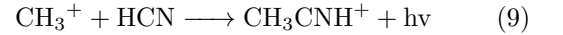
Formation of molecular species in protoplanetary disks can occur via two distinct routes: gas-phase and grain-

surface reactions, and in the case of CH_2CN both pathways are a priori possible. Based on the astrochemical disk model of [Le Gal et al. \(2019\)](#), several formation and destruction pathways are involved in the chemistry of CH_2CN . These are summarized in Table 2.

As previously mentioned, CH_3CN and CH_2CN are found to have similar excitation temperatures and morphologies, therefore it is unsurprising that they also share a comparable chemistry. Both CH_3CN and CH_2CN share a very similar grain-surface formation chemistry where both can be formed via solid state reactions with CN as follows,



([Herbst 1985](#)). From these reactions we can infer that the relative formation rates of CH_3CN and CH_2CN will depend on the relative abundance of CH_2 and CH_3 radicals on the grain surface. The similarities extend beyond these grain-surface reactions, as these molecules share a common gas-phase reaction pathway. The electronic dissociative recombination of CH_3CNH^+ has been identified as the dominant contributor to the gas-phase formation of both CH_3CN and CH_2CN ([Vastel et al. 2015](#); [Loomis et al. 2018a](#)). The full reaction route, including the formation of the ion intermediate, is as follows:



([Herbst & Leung 1990](#)). This does not seem to be the main formation pathway for CH_2CN in either the model or in ‘reality’ since the electronic dissociative recombination (DR) of CH_3CNH^+ leads to a branching ratio of ~ 1.5 in favour of CH_3CN according to the Kinetic Database for Astrochemistry² (see Table 2) while we find that $\text{CH}_2\text{CN} \gg \text{CH}_3\text{CN}$. The branching ratio for this reaction is arbitrary and it is loosely based on the fact that the energy in the $\text{CH}_3\text{CN} + \text{H}$ channel is greater than the secondary dissociation energy in the $\text{CH}_2\text{CN} + 2\text{H}$ channel ([Wakelam et al. 2012](#)). In light of this, we suggest that the grain surface formation pathway is the most important source of CH_2CN in disks. A similar conclusion was made with respect to CH_3CN by ([Le Gal et al. 2019](#)) and ([Loomis et al. 2018a](#)). However, grain-surface reactions are poorly constrained both theoretically and experimentally and therefore more experimental studies need to be carried out to verify the significance of this

² <http://kida.astrophy.u-bordeaux.fr>

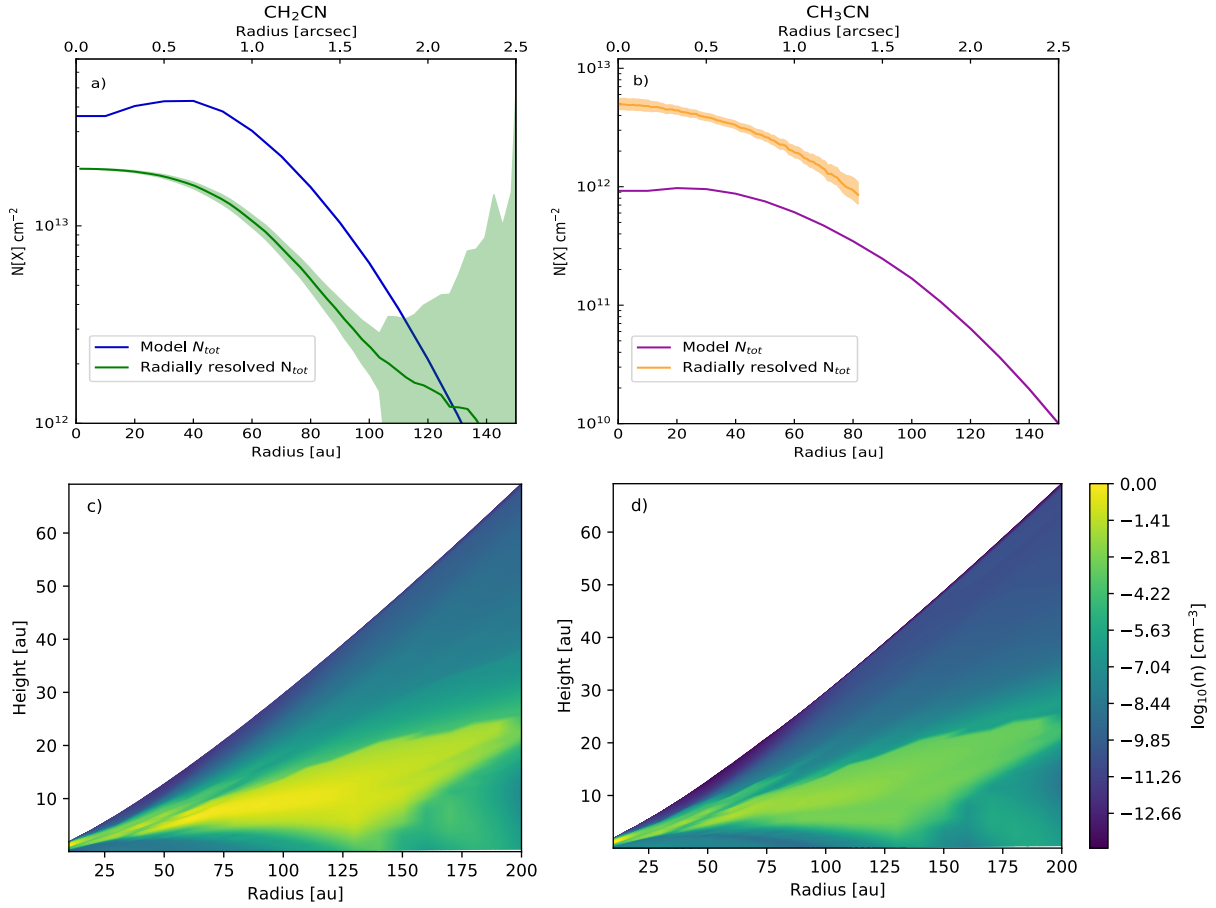


Figure 5. Panel a) & b): Total column densities of CH_2CN (a) and CH_3CN (b) as a function of radius, predicted by the chemical models of [Le Gal et al. \(2019\)](#) that we adapted to TW Hya as described in §4.1. The column density radial profile derived from the observations presented in Sect. 3.3 for CH_2CN (a) from the observation of CH_3CN obtained by [Loomis et al. \(2018a\) \(b\) are also shown. Panel c\) & d\): The abundance of \$\text{CH}_2\text{CN}\$ and \$\text{CH}_3\text{CN}\$ as a function of radius and height. The region of highest emission for both molecules is located between \$\sim 50 - 100\$ au and at a height of \$\sim 10\$ au.](#)

solid-state reaction. Finally we note that CH_2CN can also form through several neutral-neutral reactions (Table 2), whose possible contributions also warrant further investigation.

4.3. Morphology

As mentioned in Section 2.2, CH_2CN is found in a ring morphology when imaged at the native resolution of $\approx 0.3''$. The ring morphology is not unique to CH_2CN as CN and C_2H are also analogously distributed in TW Hya, however, their rings peak at considerably larger radii at ~ 45 au ($0.75''$) and 60 au ($1''$), respectively ([Bergin et al. 2016](#); [Teague & Loomis 2020](#)). These nested rings of potentially chemically related species provide clues as to what processes are regulating the abundance of these molecules. One possible source of rings is the increased penetration of UV radiation beyond the edge of the dust continuum, leading to more photo-desorption of frozen out molecules

from grain surfaces ([Cleeves 2016](#)). However, the edge of the dust continuum is at ~ 60 au, which is inconsistent with the peak of the CH_2CN ring (~ 24 au) therefore this is not a plausible explanation for the morphology of CH_2CN .

The chemical model results for CH_2CN shown in Figure 4.2 seem to replicate the morphology that we observed in Figure 4C. This suggests the presence of a ‘Goldilocks zone’ for the dominant formation pathway where the observed morphology can be attributed to the balance between formation and destruction reactions under fiducial disk conditions. Within this zone of the disk, the conditions may be particularly favourable for the production of CH_2CN (i.e. optimal UV radiation flux or temperature of the disk molecular layer).

Another possible factor that could shape the distribution of CH_2CN is enhanced destruction in the inner disk due to reactions with gas-phase carbon and oxygen atoms. Chemical modeling by [Du et al. \(2015\)](#) has

shown that C and O depletion is needed to reproduce the observed molecular abundances of CO and H₂O in TW Hya. Further, nitrile column density is enhanced by ~ 2 orders of magnitude where C and O depletion takes place (Du et al. 2015). One disk location that may present a rapid change in the C and O abundance is the CO snowline, where CO ice sublimates back into the gas-phase. The CO snowline zone in TW Hya is found at 17-30 au (Schwarz et al. 2016; Qi et al. 2013). We find that CH₂CN peaks at ~ 24 au, so the CO snowline and the CH₂CN peak may reflect the presence of C- and O-depleted gas just exterior to the CO snowline. Exterior to this region, carbon and oxygen would primarily exist as CO ice, therefore not interfere with nitrile chemistry.

5. SUMMARY

We have presented the first detection of CH₂CN (cyanomethyl) in a protoplanetary disk. The 6 emission lines detected correspond to 6 transitions of CH₂CN in its ortho state. We find a disk-averaged rotational temperature of 40 ± 5 K and a disk-averaged total column density of $(6.3 \pm 0.5) \times 10^{12} \text{ cm}^{-2}$. Assuming a thermal ortho/para ratio of 3:1, we infer a total CH₂CN column density of $(8.4 \pm 0.7) \times 10^{12} \text{ cm}^{-2}$. The molecule is observed to be in a ring whereas at lower spatial resolutions it presents a centrally-peaked profile consistent with pre-

viously reported CH₃CN morphology. Comparison with CH₃CN total column density shows that CH₂CN is 10 times more abundant. This result is consistent with chemical models for TW Hya, where CH₂CN \gg CH₃CN at all disk radii. We identify possible pathways that contribute to the formation and destruction of this molecule and we suggest that grain-surface reactions are the likely formation pathway for both CH₂CN and CH₃CN.

ACKNOWLEDGMENTS

We thank the anonymous referees for their valuable input in clarifying the results presented in this paper. We also wish to thank Ryan Loomis for sharing radial profiles of CH₃CN. This paper makes use of the following ALMA data: ADS/JAO.ALMA#2018.A.00021. ALMA is a partnership of ESO (representing its member states), NSF (USA) and NINS (Japan), together with NRC (Canada), MOST and ASIAA (Taiwan), and KASI (Republic of Korea), in cooperation with the Republic of Chile. The Joint ALMA Observatory is operated by ESO, AUI/NRAO and NAOJ. The National Radio Astronomy Observatory is a facility of the National Science Foundation operated under cooperative agreement by Associated Universities, Inc. AC acknowledges funding from the Origins of Life Initiative. This work was supported by an award from the Simons Foundation (SCOL # 321183, KÖ).

REFERENCES

- Agúndez, M., Fonfria, J. P., Cernicharo, J., Pardo, J. R., & Guélin, M. 2008, *A&A*, 479, 493, doi: [10.1051/0004-6361:20078956](https://doi.org/10.1051/0004-6361:20078956)
- Altwegg, K., Balsiger, H., Hänni, N., et al. 2020, *Nature Astronomy*, 4, 533, doi: [10.1038/s41550-019-0991-9](https://doi.org/10.1038/s41550-019-0991-9)
- Andrews, S. M., Wilner, D. J., Hughes, A. M., et al. 2012, *ApJ*, 744, 162, doi: [10.1088/0004-637X/744/2/162](https://doi.org/10.1088/0004-637X/744/2/162)
- Andrews, S. M., Huang, J., Pérez, L. M., et al. 2018, *ApJL*, 869, L41, doi: [10.3847/2041-8213/aaf741](https://doi.org/10.3847/2041-8213/aaf741)
- Bailer-Jones, C. A. L., Rybizki, J., Founesneau, M., Mantelet, G., & Andrae, R. 2018, *AJ*, 156, 58, doi: [10.3847/1538-3881/aacb21](https://doi.org/10.3847/1538-3881/aacb21)
- Bergin, E. A., Du, F., Cleaves, L. I., et al. 2016, *ApJ*, 831, 101, doi: [10.3847/0004-637X/831/1/101](https://doi.org/10.3847/0004-637X/831/1/101)
- Bergner, J. B., Guzmán, V. G., Öberg, K. I., Loomis, R. A., & Pegues, J. 2018, *ApJ*, 857, 69, doi: [10.3847/1538-4357/aab664](https://doi.org/10.3847/1538-4357/aab664)
- Chapillon, E., Dutrey, A., Guilloteau, S., et al. 2012, *ApJ*, 756, 58, doi: [10.1088/0004-637X/756/1/58](https://doi.org/10.1088/0004-637X/756/1/58)
- Cleaves, L. I. 2016, *ApJL*, 816, L21, doi: [10.3847/2041-8205/816/2/L21](https://doi.org/10.3847/2041-8205/816/2/L21)
- Cleaves, L. I., Bergin, E. A., Qi, C., Adams, F. C., & Öberg, K. I. 2015, *ApJ*, 799, 204, doi: [10.1088/0004-637X/799/2/204](https://doi.org/10.1088/0004-637X/799/2/204)
- Draine, B. T. 1978a, *ApJS*, 36, 595, doi: [10.1086/190513](https://doi.org/10.1086/190513)
- . 1978b, *ApJS*, 36, 595, doi: [10.1086/190513](https://doi.org/10.1086/190513)
- Du, F., Bergin, E. A., & Hogerheijde, M. R. 2015, *ApJL*, 807, L32, doi: [10.1088/2041-8205/807/2/L32](https://doi.org/10.1088/2041-8205/807/2/L32)
- Dutrey, A., Guilloteau, S., & Guélin, M. 1997, *A&A*, 317, L55
- Endres, C. P., Schlemmer, S., Schilke, P., Stutzki, J., & Müller, H. S. P. 2016, *Journal of Molecular Spectroscopy*, 327, 95, doi: [10.1016/j.jms.2016.03.005](https://doi.org/10.1016/j.jms.2016.03.005)
- Goldsmith, P. F., & Langer, W. D. 1999, *ApJ*, 517, 209, doi: [10.1086/307195](https://doi.org/10.1086/307195)
- Guzmán, V. V., Öberg, K. I., Carpenter, J., et al. 2018, *ApJ*, 864, 170, doi: [10.3847/1538-4357/aad778](https://doi.org/10.3847/1538-4357/aad778)
- Guzmán, V. V., Öberg, K. I., Loomis, R., & Qi, C. 2015, *ApJ*, 814, 53, doi: [10.1088/0004-637X/814/1/53](https://doi.org/10.1088/0004-637X/814/1/53)
- Herbst, E. 1985, *ApJ*, 291, 226, doi: [10.1086/163060](https://doi.org/10.1086/163060)
- Herbst, E., & Leung, C. M. 1990, *A&A*, 233, 177

- Herczeg, G. J., Wood, B. E., Linsky, J. L., Valenti, J. A., & Johns-Krull, C. M. 2004, *ApJ*, 607, 369, doi: [10.1086/383340](https://doi.org/10.1086/383340)
- Hily-Blant, P., Magalhaes, V., Kastner, J., et al. 2017, *A&A*, 603, L6, doi: [10.1051/0004-6361/201730524](https://doi.org/10.1051/0004-6361/201730524)
- Huang, J., Andrews, S. M., Cleeves, L. I., et al. 2018, *ApJ*, 852, 122, doi: [10.3847/1538-4357/aaa1e7](https://doi.org/10.3847/1538-4357/aaa1e7)
- Irvine, W. M., Friberg, P., Hjalmarsen, A., et al. 1988, *ApJL*, 334, L107, doi: [10.1086/185323](https://doi.org/10.1086/185323)
- Jones, E., Oliphant, T., & Peterson, P. 2001
- Kastner, J. H., Zuckerman, B., Weintraub, D. A., & Forveille, T. 1997, *Science*, 277, 67, doi: [10.1126/science.277.5322.67](https://doi.org/10.1126/science.277.5322.67)
- Le Gal, R., Brady, M. T., Öberg, K. I., Roueff, E., & Le Petit, F. 2019, *ApJ*, 886, 86, doi: [10.3847/1538-4357/ab4ad9](https://doi.org/10.3847/1538-4357/ab4ad9)
- Le Gal, R., Herbst, E., Xie, C., Li, A., & Guo, H. 2016, *A&A*, 596, A35, doi: [10.1051/0004-6361/201629107](https://doi.org/10.1051/0004-6361/201629107)
- Le Gal, R., Xie, C., Herbst, E., et al. 2017, *A&A*, 608, A96, doi: [10.1051/0004-6361/201731566](https://doi.org/10.1051/0004-6361/201731566)
- Liszt, H., Gerin, M., Beasley, A., & Pety, J. 2018, *ApJ*, 856, 151, doi: [10.3847/1538-4357/aab208](https://doi.org/10.3847/1538-4357/aab208)
- Loomis, R. A., Cleeves, L. I., Öberg, K. I., et al. 2018a, *ApJ*, 859, 131, doi: [10.3847/1538-4357/aac169](https://doi.org/10.3847/1538-4357/aac169)
- Loomis, R. A., Öberg, K. I., Andrews, S. M., et al. 2018b, *AJ*, 155, 182, doi: [10.3847/1538-3881/aab604](https://doi.org/10.3847/1538-3881/aab604)
- McGuire, B. A. 2018, *ApJS*, 239, 17, doi: [10.3847/1538-4365/aac5d2](https://doi.org/10.3847/1538-4365/aac5d2)
- McMullin, J. P., Waters, B., Schiebel, D., Young, W., & Golap, K. 2007, in *Astronomical Society of the Pacific Conference Series*, Vol. 376, *Astronomical Data Analysis Software and Systems XVI*, ed. R. A. Shaw, F. Hill, & D. J. Bell, 127
- Müller, H. S. P., Thorwirth, S., Roth, D. A., & Winnewisser, G. 2001, *A&A*, 370, L49, doi: [10.1051/0004-6361:20010367](https://doi.org/10.1051/0004-6361:20010367)
- Mumma, M. J., & Charnley, S. B. 2011, *ARA&A*, 49, 471, doi: [10.1146/annurev-astro-081309-130811](https://doi.org/10.1146/annurev-astro-081309-130811)
- Nomura, H., Tsukagoshi, T., Kawabe, R., et al. 2016, *ApJL*, 819, L7, doi: [10.3847/2041-8205/819/1/L7](https://doi.org/10.3847/2041-8205/819/1/L7)
- Öberg, K. I. 2016, arXiv e-prints, arXiv:1609.03112. <https://arxiv.org/abs/1609.03112>
- Öberg, K. I., & Bergin, E. A. 2020, arXiv e-prints, arXiv:2010.03529. <https://arxiv.org/abs/2010.03529>
- Öberg, K. I., Guzmán, V. V., Furuya, K., et al. 2015, *Nature*, 520, 198, doi: [10.1038/nature14276](https://doi.org/10.1038/nature14276)
- Patel, B. H., Percivalle, C., Ritson, D. J., Duffy, C. D., & Sutherland, J. D. 2015, *Nature Chemistry*, 7, 301, doi: [10.1038/nchem.2202](https://doi.org/10.1038/nchem.2202)
- Powner, M. W., Gerland, B., & Sutherland, J. D. 2009, *Nature*, 459, 239, doi: [10.1038/nature08013](https://doi.org/10.1038/nature08013)
- Qi, C., Kessler, J. E., Koerner, D. W., Sargent, A. I., & Blake, G. A. 2003, *ApJ*, 597, 986, doi: [10.1086/378494](https://doi.org/10.1086/378494)
- Qi, C., Öberg, K. I., Wilner, D. J., et al. 2013, *Science*, 341, 630, doi: [10.1126/science.1239560](https://doi.org/10.1126/science.1239560)
- Schwarz, K. R., Bergin, E. A., Cleeves, L. I., et al. 2016, *ApJ*, 823, 91, doi: [10.3847/0004-637X/823/2/91](https://doi.org/10.3847/0004-637X/823/2/91)
- Shirley, Y. L. 2015, *PASP*, 127, 299, doi: [10.1086/680342](https://doi.org/10.1086/680342)
- Teague, R. 2019a, *The Journal of Open Source Software*, 4, 1632, doi: [10.21105/joss.01632](https://doi.org/10.21105/joss.01632)
- . 2019b, *Research Notes of the AAS*, 3, 74, doi: [10.3847/2515-5172/ab2125](https://doi.org/10.3847/2515-5172/ab2125)
- Teague, R., & Loomis, R. 2020, *ApJ*, 899, 157, doi: [10.3847/1538-4357/aba956](https://doi.org/10.3847/1538-4357/aba956)
- van Dishoeck, E. F. 1994, in *Astronomical Society of the Pacific Conference Series*, Vol. 58, *The First Symposium on the Infrared Cirrus and Diffuse Interstellar Clouds*, ed. R. M. Cutri & W. B. Latter, 319
- Vastel, C., Yamamoto, S., Lefloch, B., & Bachiller, R. 2015, *A&A*, 582, L3, doi: [10.1051/0004-6361/201527153](https://doi.org/10.1051/0004-6361/201527153)
- Wakelam, V., Herbst, E., Loison, J. C., et al. 2012, *ApJS*, 199, 21, doi: [10.1088/0067-0049/199/1/21](https://doi.org/10.1088/0067-0049/199/1/21)
- Walsh, C., Loomis, R. A., Öberg, K. I., et al. 2016, *ApJL*, 823, L10, doi: [10.3847/2041-8205/823/1/L10](https://doi.org/10.3847/2041-8205/823/1/L10)
- Woon, D. E., & Herbst, E. 2009, *ApJS*, 185, 273, doi: [10.1088/0067-0049/185/2/273](https://doi.org/10.1088/0067-0049/185/2/273)